

Modelling aerodynamic forces and torques of spheroid particles in compressible flows

Yibin Du^{b,a}, Ming Yu^a, Chongwen Jiang^b, Xianxu Yuan^a

^a*State Key Laboratory of Aerodynamics, Mianyang, 621000, China*

^b*National Laboratory for Computational Fluid Dynamics, School of Aeronautic Science and Engineering, Beihang University, Beijing, 100191, China*

Abstract

In the present study, we conduct numerical simulations of compressible flows around spheroid particles, for the purpose of refining empirical formulas for drag force, lift force, and pitching torque acting on them. Through an analysis of approximately a thousand numerical simulation cases spanning a wide range of Mach numbers, Reynolds numbers and particle aspect ratios, we first identify the crucial parameters that are strongly correlated with the forces and torques via Spearman correlation analysis, based on which the empirical formulas for the drag force, lift force and pitching torque coefficients are refined. The novel formulas developed for compressible flows exhibit consistency with their incompressible counterparts at low Mach number limits and, moreover, yield accurate predictions with average relative errors of less than 5%. This underscores their robustness and reliability in predicting aerodynamic loads on spheroidal particles under various flow conditions.

Keywords: Spheroid particles, Drag force, Lift force, Pitching torque

1. Introduction

Particle-laden compressible flows are frequently encountered in natural and engineering applications. In aerospace engineering, the impact of gas during the powered landing of a spacecraft can expel dust and debris, potentially causing significant damage to high-speed vehicles (Capecelatro and Wagner, 2024). When the particle sizes are significantly smaller than the characteristic length scales of fluid motion, and the total volume fraction of the particle phase is low, the simulations of particle-laden flows can be achieved using the Eulerian-Lagrangian point-particle method. This method has found extensive application in various turbulence scenarios, including wall turbulence (Cui et al., 2023; Marchioli et al., 2016; Zhao et al., 2015, 2014), isotropic turbulence (Bounoua et al.,

Email addresses: yum16@tsinghua.org.cn (Ming Yu), yuanxianxu2023@163.com (Xianxu Yuan)

2018; Gustavsson et al., 2014), and homogeneous shear turbulence (Huang et al., 2012; Rosén et al., 2014).

In solving the particle-laden flows with the Eulerian-Lagrangian point-particle method, the accurate modeling of the forces acting on particles stands out as a critical challenge. Amongst the prevalent models, the drag force model tailored for spherical particles in incompressible flows holds a prominent position. Given the inherently small size of the particles, the particle Reynolds numbers, defined as $Re_p = \rho_f u_p d_p / \mu_f$ (where ρ_f and μ_f represent the fluid density and dynamic viscosity, $u_p = |u_f - v|$ and d_p denote the particle's slip velocity and diameter, u_f and v are the velocity of fluid and particles respectively), remain relatively low. Therefore, the Stokes drag force is dominant, rendering the inertial effects negligible. For higher Re_p values, Clift and Gauvin (1971) devised a formula for the drag on spherical particles in incompressible scenarios, drawing upon a synthesis of experimental data and insights from Stokes (1901) and Schiller and Naumann (1933). This formula is deemed applicable for Re_p values below 2×10^5 .

For non-spherical particles, there will be not only the drag force, but also lift force and pitching torque acting on them, even in the uniform incoming flow. The forces and torques acting on spheroidal particles in such flows were initially determined by Oberbeck (1876), followed by the refinement of theoretical equations for these forces in Stokes flows in subsequent studies (Batchelor, 1970; Brenner, 1961, 1964). Analytical expressions for the lift and drag coefficients of spheroidal particles under creeping flow conditions were provided by Happel and Brenner (1983). Empirical formulas for higher Reynolds numbers have been developed in recent years by many researchers (Fröhlich et al., 2020; Hölzer and Sommerfeld, 2008; Ouchene, 2020; Ouchene et al., 2016; Sanjeevi et al., 2018; Zastawny et al., 2012). Hölzer and Sommerfeld (2008) established a relation for the drag coefficient of non-spherical particles with varying sphericity, which is the ratio between the surface area of the volume-equivalent sphere and the surface area of the particle under consideration. Zastawny et al. (2012) established empirical correlations for drag, lift, pitching torque and rotational torque coefficients for spheroidal particles with aspect ratios of 1.25, 2.5, and 0.2, as well as for fibrous particles with an aspect ratio of 5. Richter and Nikrityuk (2013) thoroughly examined the heat transfer, forces, and torques acting on spheroidal and cubic particles and established a comprehensive set of closure relations for heat flow and flow through nonspherical particles. Ouchene et al. (2016) conducted direct numerical simulations of symmetric particle bypass flows and proposed empirical formulations for the lift, drag, and pitching torque coefficients of spheroidal particles with aspect ratios ranging from 1 to 32 at the Reynolds number ranging from 0.1 to 240. The fitted formulas are further corrected by Arcen et al. (2017). Sanjeevi et al. (2018) considered spheroidal particles with the aspect ratios of $w = 2.5, 0.4$, and fibrous

particles with $w = 4$. The simulations covered a wide range of Reynolds numbers from 0.1 to 2000. Fröhlich et al. (2020) studied the flow separation conditions of prolate spheroid particles with aspect ratios ranging from 1 to 8 at the Reynolds number from 1 to 100, resulting in the development of new empirical expressions for the drag, lift, and torque of these particles. Ouchene (2020) investigated the forces acting on oblate spheroidal particles with shape factors ranging from 0.2 to 1. The resulting expressions for lift, drag, and pitching torque coefficients are applicable within the range of $Re_p < 100$.

In the realm of compressible flows, experimental data indicates the significance of compressibility effects (Nagata et al., 2016). The particle Mach number $M_p = u_p/a_f$ (where a_f represents the sound speed of ambient fluid) serves as a crucial parameter for assessing the impacts of flow compressibility. Loth (2008) investigated the drag of spherical particles in compressible flows, noting a weak Mach number effect below the critical Mach number ($M_p < 0.6$) and a nearly constant drag coefficient in the hypersonic regime ($M_p > 5$). Subsequently, Parmar et al. (2010) identified limitations in the fitting formula proposed by Loth (2008) through an analysis of data from Bailey and Starr (1976), offering an enhanced correlation for the drag coefficient of a sphere in compressible flows. Loth et al. (2021) developed empirical expressions for a broader range of Re_p and M_p using numerical simulations and past experimental data, significantly enhancing their accuracy and applicability.

The brief literature review above highlights the extensive development and validation of forcing models for spherical particles in both incompressible and compressible flows, as well as for non-spherical particles in incompressible flows. However, empirical formulas for the drag force, lift force, and pitching torque of non-spherical particles in compressible flows are currently lacking, to the best of our knowledge. This serves as the primary motivation for the current study. This paper aims to investigate the forces and torques acting on spheroidal particles with varying aspect ratios at different Mach numbers ($M_p \leq 2$) and Reynolds numbers ($10 \leq Re_p \leq 100$) via numerical simulations, where vortex shedding will not occur. Based on these simulations, empirical formulas for drag, lift force, and pitching torque will be developed.

The remainder of this paper is organized as follows. In section 2 we introduce the numerical method employed in the present study as well as its validation. In section 3 we discuss at length the variation of the drag force, lift force, and pitching torque with the Reynolds and Mach numbers for particles with different aspect ratios and the angle of attack. The empirical formulas of the forces and torque will be given correspondingly. Conclusions are recapitulated in section 4.

2. Numerical methods and validation

In this study, we consider compressible Newtonian perfect gas flowing around small-sized particles in the shape of axisymmetric ellipsoids, namely the spheroids. The forces acting on these particles are influenced by several parameters, including the particle Mach number M_p , the particle Reynolds number Re_p , the aspect ratio of the particle w , and the angle of attack α . The aspect ratio is defined as $w = a/b$, where a denotes the length of the spheroid's axis of rotational symmetry, and b represents the length of the other two identical axes. Particles are classified as 'prolate' when $w > 1$ and 'oblate' when $w < 1$. The angle of attack, denoted by α , is defined as the angle between the long axis of the spheroid and the direction of the incoming flow.

The coordinate system is established with its origin at the center of the particle. The x -axis aligns parallel to the direction of the incoming flow, while the z -axis is oriented perpendicularly to the plane formed by long axis orientation and the x axis. The y -axis is determined according to the right-hand rule of the coordinate system. In the cases where the angle of attack equals zero, and the flow around the particles remains steady, the flow exhibits axisymmetry relative to the x axis for prolate particles, rendering the y and z directions equivalent, while the flow is only symmetrical relative to the $z = 0$ plane for oblate particles.

Numerical simulations are conducted using the NNW-PHengLEI software developed by the China Aerodynamics Research and Development Center (He et al., 2016). The compressible Navier-Stokes equations are solved by the finite volume method. The convection terms are approximated using the Roe scheme, the viscous terms are computed by the central difference scheme, and time advancement is achieved using the implicit LU-SGS method. The mesh grid configuration is depicted in Figure 1, using the particle with $w = 2.5$ as an example. The computational domain is half of a sphere with a diameter of $20a$, which is considered to have minimal impact on particle forces (Richter and Nikrityuk, 2012). The initial grid spacing is set at $0.005a$ in the first mesh layer to ensure precise computation of viscous stresses, thereafter expanding by 1.05 times within $4a$ and by 1.2 times outward. The total cell count varies between 0.7 and 1.2 million cells across different scenarios, depending on the shapes of particles.

To validate the accuracy of the numerical techniques employed in this study, we firstly conduct simulations for the flows around prolate spheroid particles with $w = 2.5$ and oblate spheroid particles with $w = 0.4$ at $Re_p = 10$ and 100 in low Mach number $M_p = 0.1$ for comparison with incompressible flows. The angle of attack α varies from 0° to 90° . We primarily compare the drag force F_D , lift force F_L and pitching torque T , calculated as

$$F_D = - \int_S p \mathbf{e}_x \cdot \mathbf{n} dS + \int_S \mathbf{n} \cdot \boldsymbol{\tau} \cdot \mathbf{e}_x dS \quad (1)$$

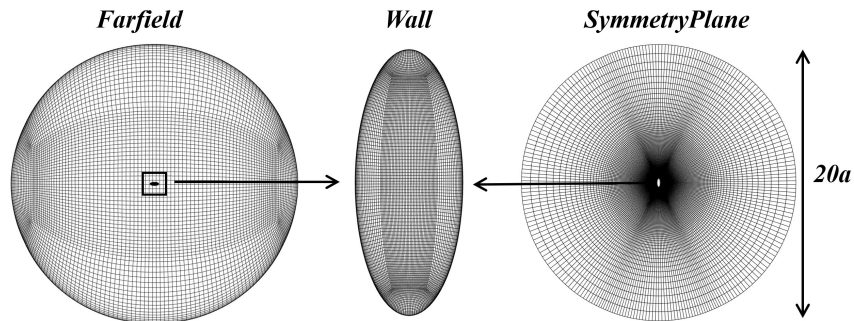


Figure 1: Sketch of computational domain and mesh grids for particles with $w = 2.5$ at the far field (left), the wall (middle), and the symmetry plane(right).

$$F_L = - \int_S p \mathbf{e}_y \cdot \mathbf{n} dS + \int_S \mathbf{n} \cdot \boldsymbol{\tau} \cdot \mathbf{e}_y dS \quad (2)$$

$$T = |(F_D \mathbf{e}_x + F_L \mathbf{e}_y) \times \mathbf{r}_{cp}| \quad (3)$$

where p is the pressure, $\boldsymbol{\tau}$ is the viscous stress tensor, \mathbf{e}_x and \mathbf{e}_y are the unit vector in the x and y directions, \mathbf{n} is the unit vector at the particle surface, and \mathbf{r}_{cp} is location of the pressure center. Correspondingly, the drag force coefficient C_D , lift force coefficient C_L , and pitching torque coefficient C_T are defined as

$$C_D = \frac{8F_D}{\rho_\infty \pi d_p^2 U_\infty^2}, \quad C_L = \frac{8F_L}{\rho_\infty d_p^2 U_\infty^2}, \quad C_T = \frac{16T}{\rho_\infty \pi d_p^3 U_\infty^2} \quad (4)$$

where ρ_∞ and U_∞ are the density and velocity of the incoming flow, respectively. The d_p denotes diameter of the volume-equivalent sphere for non-spherical particles.

The results are shown in Figure 2, along with the empirical formulas and simulation data presented by Ouchene et al. (2016); Sanjeevi et al. (2018); Zastawny et al. (2012) and Ouchene (2020). In Figure 2(a,b), we divide C_D by $C_{D,\alpha=0^\circ}$ to enhance their clarity in showing the trend of variation, where $C_{D,\alpha=0^\circ}$ is also given by the present simulation, and a similar approach is employed in subsequent contents of this paper. The relative discrepancies in comparison to these formulas are detailed in Table 1. Overall, the current results align well with these empirical formulas and simulation data. Notably, the deviations from the results of Sanjeevi et al. (2018) are minimal, with an average relative error generally less than 2.5%. Conversely, the simulation data by Ouchene et al. (2016, 2015) and Ouchene (2020) demonstrate higher relative errors, notably 12% for drag and 16% for lift coefficients, and empirical correlations presented by Ouchene et al. (2016) and Ouchene (2020) give the average relative errors of approximately 10% for drag, lift and pitching torque coefficients comparing with the present results. For the numerical results calculated by Zastawny et al. (2012), the average relative error for drag and lift

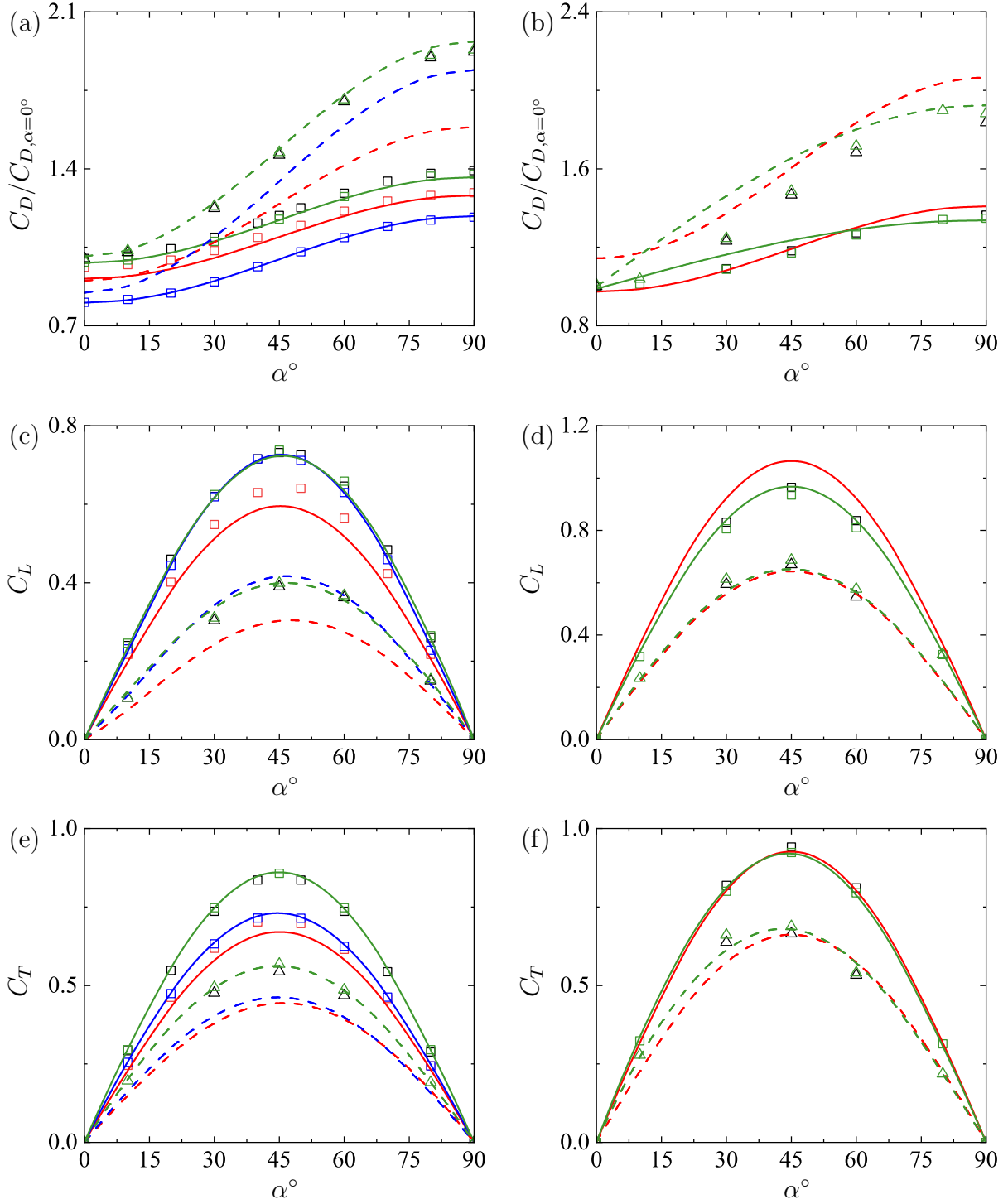


Figure 2: Variation of (a,b) $C_D/C_{D,\alpha=0^\circ}$, (c,d) C_L and (e,f) C_T against the angle of attack α , at $M_p = 0.1$. (a,c,e) $w = 2.5$, (b,d,f) $w = 0.4$. Solid lines: empirical formulas at $Re_p = 10$, dashed lines: empirical formulas at $Re_p = 100$. Squares: simulation at $Re_p = 10$, triangles: simulation at $Re_p = 100$. Black lines and symbols: present results, red lines and symbols: (a,c,e) Ouchene et al. (2016), (b,d,f) Ouchene (2020), blue lines and symbols: Zastawny et al. (2012), green lines and symbols: Sanjeevi et al. (2018).

Table 1: Relative error between the simulation results at $M_p = 0.1$ and simulations and empirical correlations given by previous studies.

		Ouchene et al. (2016) Ouchene (2020)	Zastawny et al. (2012)	Sanjeevi et al. (2018)	
Simulations	C_D	Mean(%)	5.69	11.86	1.06
		Max(%)	7.14	16.23	2.44
	C_L	Mean(%)	12.41	9.00	2.47
		Max(%)	16.50	11.99	5.24
	C_T	Mean(%)	15.96	1.93	2.58
		Max(%)	16.40	3.78	4.21
Correlations	C_D	Mean(%)	9.24	13.45	1.91
		Max(%)	17.39	19.74	4.55
	C_L	Mean(%)	11.09	3.49	1.13
		Max(%)	22.46	6.13	2.14
	C_T	Mean(%)	10.40	14.50	2.20
		Max(%)	20.96	15.09	3.10

Table 2: Relative error between the simulation and previous results for spherical particles

		Loth et al. (2021)	Nagata et al. (2016)
Mean(%)	$Re_p = 50$	7.29	2.34
	$Re_p = 100$	8.04	2.92
Max(%)	$Re_p = 50$	15.17	3.95
	$Re_p = 100$	15.21	4.36
Mean(%)	All cases	7.66	2.63

coefficients is approximately 10%, while the error for torque coefficients is only 2%. The correlations by Zastawny et al. (2012) give the average relative error of approximately 14% for drag and torque coefficients, and 3.5% for lift coefficients. These discrepancies can probably be attributed to the numerical simulation methodologies employed in these studies. As a result, we consider that the numerical approach adopted is deemed valid for low Mach number flows.

We also perform simulations for flow past spherical particles at higher Mach numbers M_p ranging from 0.3~2.0. The drag coefficients C_D are compared with the direct numer-

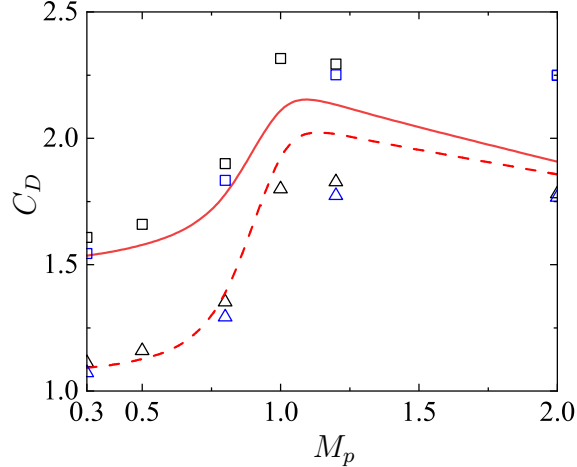


Figure 3: Variation of C_D against M_p , at $w = 1$. Black symbols: present simulations, blue symbols: Nagata et al. (2016). Red lines: empirical formula proposed by Loth et al. (2021). Squares and solid lines: $Re_p = 50$, triangles and dashed lines: $Re_p = 100$.

ical simulation (DNS) results of Nagata et al. (2016) and the empirical formula proposed by Loth et al. (2021), as illustrated in Figure 3. The relative errors are reported in Table 2. With the increasing M_p , the C_D values initially rise and then decline, peaking around $M_p \approx 1$. While this trend aligns with the fitting formula by Loth et al. (2021), discrepancies exist, with higher values compared to the latter at $Re_p = 50$ and lower at $Re_p = 100$. The average relative error stands at approximately 7%. The DNS results from Nagata et al. (2016) slightly undershoot the present findings, with an average relative error below 3%. These relatively minor discrepancies underscore the validity of the numerical methodology employed in this study.

Lastly, we evaluate the influences of grid quality on the numerical results using the simulation cases listed in Table 3. Four grid types with different minimal grid sizes, cell numbers and the use of full/half model were compared at $Re_p = 10, 100$ and $\alpha = 45^\circ$ for prolate spheroids with $w = 2.5$. The relative errors between these cases and the numerical results of Sanjeevi et al. (2018) are lower than 4%, and the relative differences amongst the present results are less than 0.45%, thereby validating the appropriateness of the grid settings herein.

3. Forces and torques on spheroid particles

As we have stated in the previous section, the forces and torques acting on the spheroid particles may be influenced by several factors, including the particle Reynolds number Re_p , the particle Mach numbers M_p , the aspect ratio w and the angle of attack α . To fully understand the effects of these parameters and establish the model for the forces

Table 3: Drag force, lift force and pitching torque coefficients of spheroid with $w = 2.5$ at $\alpha = 45^\circ$, $Re_p = 10$ and 100 and $M_p = 0.1$.

Re_p	Total cells	Model	Minimum grid interval	C_D	C_L	C_T	Max relative error(%)
10	668334	half	0.01a	4.5764	0.7335	0.8490	0.451
	884520	half	0.005a	4.5618	0.7318	0.8488	
	1997960	half	0.001a	4.5810	0.7340	0.8489	
	1916398	whole	0.005a	4.5825	0.7340	0.8488	
	Sanjeevi et al. (2018)			4.4984	0.7382	0.8571	
100	668334	half	0.01a	1.1764	0.3894	0.5458	0.220
	884520	half	0.005a	1.1780	0.3900	0.5457	
	1997960	half	0.001a	1.1759	0.3891	0.5460	
	1916398	whole	0.005a	1.1767	0.3892	0.5458	
	Sanjeevi et al. (2018)			1.1780	0.3987	0.5679	

and torques, we consider six groups of spheroidal particles with different aspect ratios under various incoming flow conditions. The aspect ratio w ranges from 0.2 to 5.0. The Re_p covers the range of $10 \sim 100$ and M_p from $0.1 \sim 2.0$. The angle of attack α is set as 0° , 30° , 45° , 60° and 90° , respectively. The database considered herein encompasses 960 groups of simulation results. The majority of simulations exhibit the Knudsen number below 0.1, indicating that the rarefaction of flow can be effectively disregarded.

As a first impression of the flow field, in Figure 4, we present the distributions of the relative pressure $(p - p_\infty)/p_\infty$ and the streamlines near the spanwise symmetrical plane in the cases at $Re_p = 50$ and $M_p = 0.3, 1.0$ and 2.0 for particles with $w = 2.5$ and 0.4 at $\alpha = 45^\circ$. For prolate particles with $w = 2.5$ at $M_p = 0.3$, the streamlines originating from the upstream travel around the solid wall and extend to the leeward side of the particle, forming a small reverse flow region. The pressure is highest at the stagnation point and decreases in regions with higher shear rates, aligning with incompressible flow results (Fröhlich et al., 2020; Ouchene, 2020; Ouchene et al., 2016, 2015; Sanjeevi et al., 2018; Zastawny et al., 2012), indicating insignificant compressibility effects. The pressure distribution lacks symmetry about its main axis or mass center, implying the non-zero lift force and pitching torque. At $M_p = 1.0$, a normal shock is evident due to increased flow compression, as indicated by a strong pressure gradient in the vicinity of the particle.

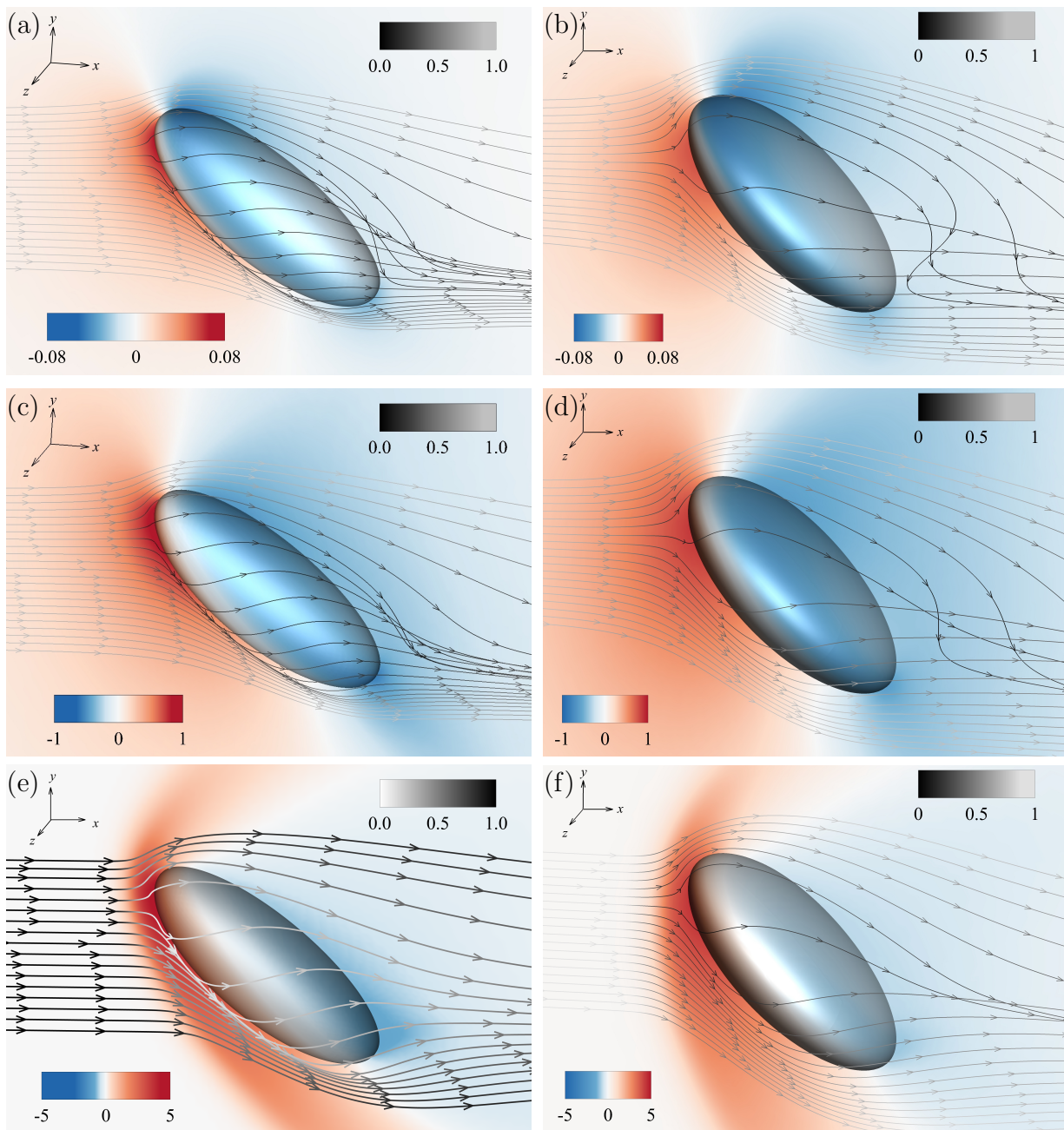


Figure 4: Distribution of relative pressure $(p-p_\infty)/p_\infty$ and the streamlines colored by streamwise velocity at $Re_p = 50$ and $\alpha = 45^\circ$ at different Mach numbers, (a,b) $M_p = 0.3$, (c,d) $M_p = 1$, (e,f) $M_p = 2$, (a,c,e) $w = 2.5$, (b,d,f) $w = 0.4$.

At $M_p = 2.0$, the shock wave detaches from the particle, creating a region of high pressure ahead of the particle and downstream of the shock wave, leading to high-pressure drag. Despite the identical Reynolds numbers Re_p , the reverse flow regions in these higher M_p cases are notably smaller, suggesting that higher Mach numbers alleviate flow separation. Additionally, the asymmetrical pressure distribution highlights an enhanced pitching torque. Similar observations are made for oblate particles with $w = 0.4$, except that the stronger flow separations and higher pressure behind the detached shock imply increased pressure drag, lift force, and pitching torque.

3.1. Drag force

In this subsection, we investigate the variation of the drag force with the four key parameters stated above. It is necessary to recall first the empirical formula of the drag coefficient for incompressible flows. Happel and Brenner (1983) provided an analytical drag expression for spheroidal particles in creeping flows, which was subsequently summarized by Ouchene (Ouchene, 2020; Ouchene et al., 2016). For prolate spheroidal particles with $w > 1$, the drag coefficient C_D at the attack angle of $\alpha = 0^\circ$ and $\alpha = 90^\circ$ are given by

$$C_{D,Stokes,\alpha=0^\circ}(Re_p, w) = \frac{64}{Re_p} w^{-1/3} \left[\frac{-2w}{w^2 - 1} + \frac{2w^2 - 1}{(w^2 - 1)^{3/2}} \ln \left(\frac{w + \sqrt{w^2 - 1}}{w - \sqrt{w^2 - 1}} \right) \right]^{-1}, \quad (5)$$

$$C_{D,Stokes,\alpha=90^\circ}(Re_p, w) = \frac{64}{Re_p} w^{-1/3} \left[\frac{w}{w^2 - 1} + \frac{2w^2 - 3}{(w^2 - 1)^{3/2}} \ln(w + \sqrt{w^2 - 1}) \right]^{-1}, \quad (6)$$

while for oblate particles with $w < 1$, the drag coefficient C_D are expressed as follows,

$$C_{D,Stokes,\alpha=0^\circ}(Re_p, w) = \frac{64}{Re_p} w^{-1/3} \left[\frac{-w}{1 - w^2} - \frac{2w^2 - 3}{(1 - w^2)^{3/2}} \arcsin(\sqrt{1 - w^2}) \right]^{-1}, \quad (7)$$

$$C_{D,Stokes,\alpha=90^\circ}(Re_p, w) = \frac{64}{Re_p} w^{-1/3} \left[\frac{2w}{1 - w^2} + \frac{2(1 - 2w^2)}{(1 - w^2)^{3/2}} \arctan\left(\frac{\sqrt{1 - w^2}}{w}\right) \right]^{-1}. \quad (8)$$

At higher Re_p , Reynolds number effects should be considered. Our study primarily considers the formula proposed by Fröhlich et al. (2020), incorporating a correction factor $f_{d,\alpha}$ for prolate particles at $\alpha = 0^\circ$ and 90° ,

$$C_{D,\alpha=0^\circ}(Re_p, w) = C_{D,Stokes,\alpha=0^\circ}(Re_p, w) f_{d,\alpha=0^\circ}(Re_p, w), \quad (9)$$

$$C_{D,\alpha=90^\circ}(Re_p, w) = C_{D,Stokes,\alpha=90^\circ}(Re_p, w) f_{d,\alpha=90^\circ}(Re_p, w), \quad (10)$$

where the correction factor $f_{d,\alpha}$ for the drag coefficient at $\alpha = 0^\circ$ and 90° of prolate particles are

$$f_{d,\alpha=0^\circ}(Re_p, w) = 1 + 0.15 Re_p^{0.687} + c_{d,1} (\ln w)^{c_{d,2} Re_p^{c_{d,3} + c_{d,4} \ln w}}, \quad (11)$$

Table 4: Parameters $c_{d,i}$ in Eq. (11) and (12).

	$i = 1$	$i = 2$	$i = 3$	$i = 4$	$i = 5$	$i = 6$	$i = 7$	$i = 8$
$w > 1$	-0.0045	1.742	1.436	-0.2181	0.05274	0.697	0.5813	0.0879
$w < 1$	585	-0.8002	-4.797	0.6141	0.0536	0.5335	0.6186	0.1648

Table 5: Comparison of the relative errors of the empirical formulas for C_D at $M_p = 0.1$.

		Present	Ouchene et al. (2016) Ouchene (2020)	Zastawny et al. (2012)	Sanjeevi et al. (2018)
$w > 1$	Mean(%)	2.23	12.12	12.37	1.69
	Max(%)	8.49	29.28	19.75	2.46
$w < 1$	Mean(%)	1.60	7.31	13.86	3.27
	Max(%)	15.22	22.41	29.00	15.72

$$f_{d,\alpha=90^\circ}(Re_p, w) = 1 + 0.15Re_p^{0.687} + c_{d,5}(\ln w)^{c_{d,6}Re_p^{c_{d,7}+c_{d,8}\ln w}}, \quad (12)$$

and for oblate particles, w should be replaced by $1/w$. The drag coefficient exhibits a sinusoidal function squared trend for attack angles between 0° and 90° ,

$$C_D(Re_p, w, \alpha) = C_{D,\alpha=0^\circ}(Re_p, w) + (C_{D,\alpha=90^\circ}(Re_p, w) - C_{D,\alpha=0^\circ}(Re_p, w)) \sin^2(\alpha) \quad (13)$$

which is found to have a wide range of applicability up to $Re_p = 2000$ for prolate spheroid (Sanjeevi and Padding, 2017), and maintain a specific degree of precision for oblate particles as validated by the present simulations. As w equals to 1, the formula above degenerates to the drag coefficients of spherical particles given by Schiller and Naumann (1933). The parameters in Eq. (11) and (12) are detailed in Table 4, which are obtained by data fitting using the present numerical simulation results. The relative errors are given in Table 5. In comparison to the predictions provided by previous formulas, the empirical law presented here exhibits significantly lower relative errors than those proposed by Ouchene (2020); Ouchene et al. (2016) and Zastawny et al. (2012) for all cases considered. The formula by Sanjeevi et al. (2018) shows lower mean and maximum relative errors for prolate particles, but higher errors for oblate particles, which should probably attributed to the fact that the formula for former was originally proposed only for $w = 2.5$.

We now start to incorporate compressibility effects into this formula. One approach is to introduce an additional correlation factor into the existing formulas. Nevertheless, research by Loth et al. (2021) on compressible spherical particles reveals a coupling between the particle Reynolds number Re_p and Mach number M_p . For the current spheroid particles under consideration, likely, w is also linked to M_p . To clarify this relationship,

Table 6: Spearman correlation analysis for drag force coefficients.

		Re_p	M_p	w
$w < 1$	$C_{D,\alpha=0}$	0.097	0.973	0.125
$M_p \leq 1$	$C_{D,\alpha=90}$	0.185	0.943	-0.047
$w < 1$	$C_{D,\alpha=0}$	0.854	-0.210	0.079
$M_p > 1$	$C_{D,\alpha=90}$	0.894	-0.144	-0.079
$w > 1$	$C_{D,\alpha=0}$	0.400	0.633	-0.059
$M_p \leq 1$	$C_{D,\alpha=90}$	0.537	0.590	-0.042
$w > 1$	$C_{D,\alpha=0}$	-0.944	0.104	-0.234
$M_p > 1$	$C_{D,\alpha=90}$	0.959	-0.141	-0.133

we perform Spearman correlation analysis using all simulation data. The Spearman correlation coefficients demonstrate the consistent changes in drag coefficients with these flow parameters, where ± 1 signifies a perfect monotonic correlation, whereas a value of 0 signifies the absence of a correlation. The findings, presented in Table 6, suggest that both Re_p and M_p are significant factors to be included in the empirical formula for drag force coefficients, while w is comparatively less influential.

We analyze the influence factor mathematically by considering its relationship with various variables,

$$g_{d,\alpha=0^\circ}(Re_p, M_p) = d_{0,1} Re_p^{d_{0,2}} M_p^{d_{0,3}} \quad (14)$$

$$g_{d,\alpha=90^\circ}(Re_p, M_p) = d_{90,1} Re_p^{d_{90,2}} M_p^{d_{90,3}} \quad (15)$$

The drag coefficients $C_{D,\alpha=0^\circ}$ and $C_{D,\alpha=90^\circ}$ for spheroid particles in compressible flows are, therefore, expressed as

$$C_{D,\alpha=0^\circ}(Re_p, w, M_p) = C_{D,\alpha=0^\circ}(Re_p, w) g_{d,\alpha=0^\circ}(Re_p, M_p) \quad (16)$$

$$C_{D,\alpha=90^\circ}(Re_p, w, M_p) = C_{D,\alpha=90^\circ}(Re_p, w) g_{d,\alpha=90^\circ}(Re_p, M_p) \quad (17)$$

with $C_{D,\alpha=0^\circ}(Re_p, w)$ and $C_{D,\alpha=90^\circ}(Re_p, w)$ representing the empirical formulas for incompressible flows, as given in Eq. (9) and (10). For other attack angles, C_D follows a sinusoidal function squared trend as detailed in Eq. (13). To sum up, C_D formula can be written as

$$C_D(Re_p, w, M_p, \alpha) = C_{D,\alpha=0^\circ}(Re_p, w, M_p) + (C_{D,\alpha=90^\circ}(Re_p, w, M_p) - C_{D,\alpha=0^\circ}(Re_p, w, M_p)) \sin^2(\alpha) \quad (18)$$

Table 7: Parameters $d_{0,i}$ and $d_{90,i}$ in Eq. (14) and Eq. (15) for drag coefficients and average relative errors.

		$d_{0,1}$	$d_{0,2}$	$d_{0,3}$	$d_{90,1}$	$d_{90,2}$	$d_{90,3}$	Average relative error(%)
$w > 1$	$M_p \leq 1$	1	0.07258	3.674	1	0.1022	2.792	3.11
	$M_p > 1$	0.949	0.08366	0.1941	0.7131	0.1881	-0.06457	
$w < 1$	$M_p \leq 1$	1	0.0788	3.486	1	0.1091	2.8466	2.80
	$M_p > 1$	0.8677	0.1218	-0.5433	0.7598	0.181	-0.1093	

As M_p approaches 0, the values of $g_{d,\alpha=0^\circ}$ and $g_{d,\alpha=90^\circ}$ converge to 1.0, leading to a transition to incompressible flow scenarios. The formula parameters are provided in Table 7.

In Figure 5, we illustrate the variation of drag coefficients with Mach numbers at $Re_p = 10$ and 100 for particles of different aspect ratios w . Across all shapes, drag coefficients exhibit a monotonic increase at $M_p < 1$ but experience a sudden decline at the critical point $M_p = 1$. Beyond $M_p = 1$, drag coefficients at $\alpha = 0^\circ$ for prolate particles display a non-monotonic trend with M_p , initially decreasing and then increasing, while other drag coefficients decrease monotonically at $Re_p = 10$. A similar trend of variation is observed for cases at $Re_p = 100$. The proposed empirical formulas accurately capture these trends, with an average relative error of approximately 3%, indicating their capability to predict drag coefficients for particles of varying aspect ratios w in terms of M_p .

Figure 6 illustrates the variation of the drag coefficient with the particle Reynolds number Re_p for prolate and oblate particles with aspect ratios $w = 2.5$ and 0.4, respectively, grouped by three M_p values. Across all particle aspect ratios w and M_p considered, the drag coefficients decrease monotonically with Re_p , which is well captured by the proposed formula. This behavior holds true for particles with different aspect ratios, affirming the validity of the proposed formula concerning Re_p .

Lastly, we examine the impact of the angle of attack on the drag coefficient at various Mach numbers, shown in Figure 7. The trend in drag coefficient variation is consistent for both compressible and incompressible flows, suggesting that the attack angle α plays a minor role in drag coefficient modification. Overall, the predicted C_D using the proposed formula aligns well with simulation results, validating the use of the sinusoidal function squared to derive C_D at any arbitrary attack angle α from 0° to 90° .

In this subsection, we focus on adjusting drag coefficients for spheroid particles in compressible flows. Through an examination of drag coefficient variations with Re_p , M_p , w , and α , we demonstrate that the proposed empirical formulas closely match simulation

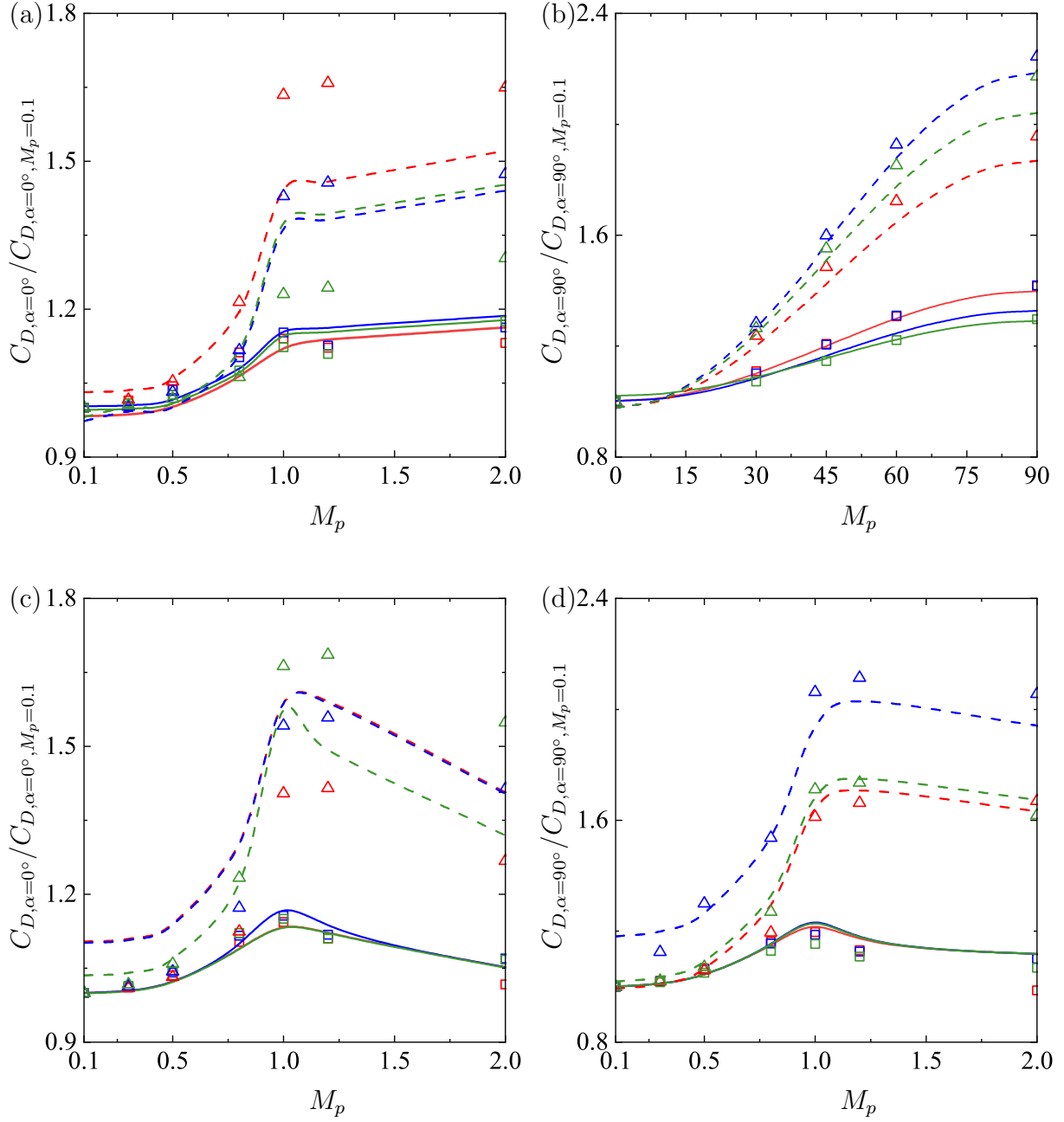


Figure 5: Variation of particle drag coefficients (a,c) $C_{D,\alpha=0^\circ}/C_{D,\alpha=0^\circ,M_p=0.1}$ and (b,d) $C_{D,\alpha=90^\circ}/C_{D,\alpha=90^\circ,M_p=0.1}$ against M_p , (a,b) prolate particles: $w = 1.25$ (red), $w = 2.5$ (blue), $w = 5$ (green) and (c,d) oblate particles: $w = 0.2$ (red), $w = 0.4$ (blue), $w = 0.8$ (green). Solid lines and squares: $Re_p = 10$, dashed lines and triangles: $Re_p = 100$. Lines: (a,c) Eq. (16), (b,d) Eq. (17), symbols: present simulations.

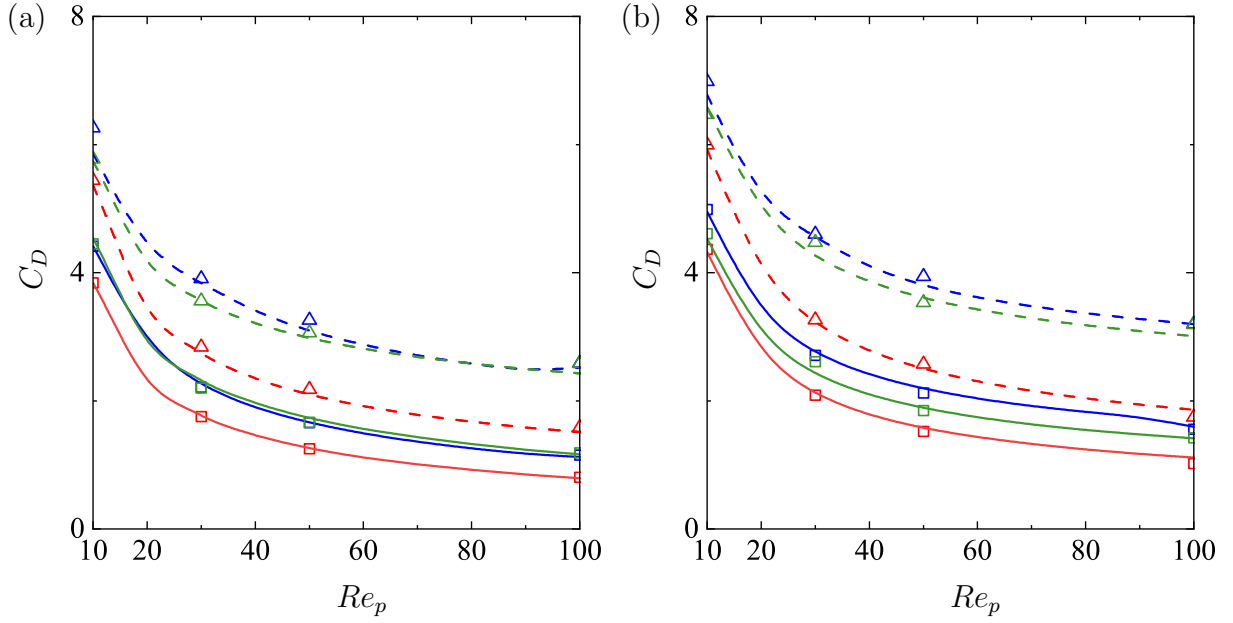


Figure 6: Variation of particle drag coefficients C_D against Re_p , (a) $w = 2.5$ and (b) $w = 0.4$. Solid lines and squares: $C_{D,\alpha=0^\circ}$, dashed lines and triangles: $C_{D,\alpha=90^\circ}$ for $M_p = 0.3$ (red), $M_p = 1.0$ (blue), $M_p = 2.0$ (green). Solid lines: Eq. (16), dashed lines: Eq. (17), symbols: present simulations.

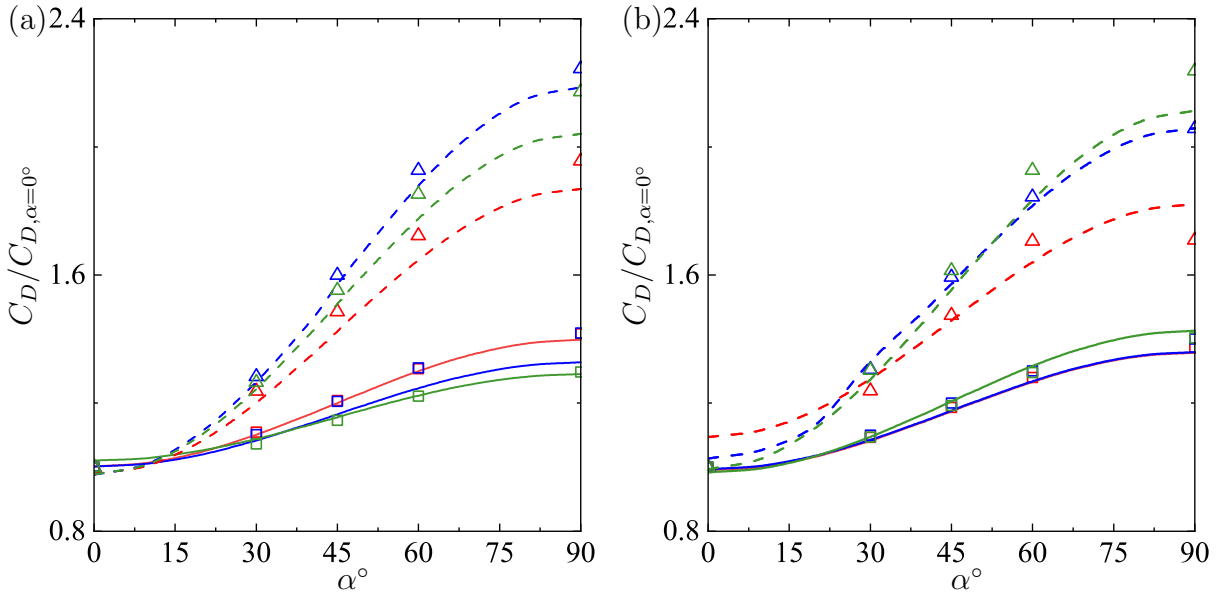


Figure 7: Variation of particle drag coefficients $C_D/C_{D,\alpha=0^\circ}$ against α , (a) $w = 2.5$ and (b) $w = 0.4$ for $M_p = 0.3$ (red), $M_p = 1.0$ (blue), $M_p = 2.0$ (green). Solid lines and squares: $Re_p = 10$, dashed lines and triangles: $Re_p = 100$. Lines: Eq. (18), symbols: present simulations.

results, with an average relative error of less than 3%.

3.2. Lift force

We further consider the lift force in this subsection. Theoretical derivations and empirical formulas for the lift force coefficients are usually associated with the modeling of their drag forces (Fröhlich et al., 2020; Ouchene, 2020; Ouchene et al., 2016), Happel and Brenner (1983) derived lift coefficients for spheroidal particles in stokes flow as follows

$$C_{L,Stokes} = (C_{D,Stokes,\alpha=90^\circ} - C_{D,Stokes,\alpha=0^\circ}) \sin(\alpha) \cos(\alpha) \quad (19)$$

coupling the drag coefficients $C_{D,Stokes,\alpha=0^\circ}$ and $C_{D,Stokes,\alpha=90^\circ}$ with trigonometric function $\sin(\alpha) \cos(\alpha)$ to determine the lift coefficients in creeping flows. To incorporate high Reynolds number effects, the maximum value of the lift coefficient reached at $\alpha = 45^\circ$ should be modified by multiplying the correction factor (Fröhlich et al., 2020) as

$$C_{L,\alpha=45^\circ}(Re_p, w) = (C_{D,Stokes,\alpha=90^\circ} - C_{D,Stokes,\alpha=0^\circ}) f_{l,\alpha=45^\circ}(Re_p, w) \quad (20)$$

with the correction factor

$$f_{l,\alpha=45^\circ}(Re_p, w) = 1 + c_{l,3} Re_p^{c_{l,4} + c_{l,5} \ln w} w^{c_{l,6} + c_{l,7} Re_p} \quad (21)$$

In creeping flows, the maximum lift coefficients are observed at $\alpha = 45^\circ$ and exhibit a symmetrical distribution as the angle approaches 0° and 90° . However, such a symmetrical variation is violated at higher Reynolds numbers. To account for the unsymmetrical shift, we propose to use the following expression,

$$C_L(Re_p, w, \alpha) = 2(\sin \alpha)^{c_{l,1}^{Re_p w}} (\cos \alpha)^{c_{l,2}^{Re_p w}} C_{L,\alpha=45^\circ}(Re_p, w) \quad (22)$$

which is based on the results of our simulation and previous studies in the field. Note that these formulas are valid for prolate particles. Those for the oblate particles can be obtained by replacing the w as $1/w$, same as the procedure employed for drag force coefficients. The correlation for lift coefficient proposed above has the same form as the theoretical solution in Eq. (19) when the particle Reynolds number Re_p approaches zero. The parameters in the formulas are listed in Table 8 obtained by the best fitting using the results at $M_p = 0.1$.

In Figure 8, we present a comparison of lift coefficients obtained from numerical simulations with empirical formulas proposed by Ouchene (2020); Ouchene et al. (2016); Zastawny et al. (2012) and Sanjeevi et al. (2018), along with the revised formula given herein. At low Reynolds numbers, the lift coefficient exhibits symmetry around $\alpha = 45^\circ$. However, for prolate spheroidal particles, increasing aspect ratios w and Reynolds numbers Re_p disrupt this symmetry, particularly pronounced at $w = 5$ and $Re_p = 100$. The

Table 8: Parameters $c_{l,i}$ in Eq. (21) and Eq. (22).

	$i = 1$	$i = 2$	$i = 3$	$i = 4$	$i = 5$	$i = 6$	$i = 7$
$w > 1$	1.0005	0.9995	0.3402	0.8787	-0.0493	0.0	0.0
$w < 1$	0.9998	1.0002	0.0600	1.1333	0.0905	0.1908	-0.0037

Table 9: Spearman correlation analysis for lift coefficient $C_{L,\alpha=45^\circ}$

	Re_p	M_p	w
$w < 1, M_p \leq 1$	0.090	0.893	0.052
$w < 1, M_p > 1$	0.864	-0.465	0.074
$w > 1, M_p \leq 1$	0.532	0.566	0.062
$w > 1, M_p > 1$	0.864	-0.427	0.112

variations of C_L against Re_p at $\alpha = 45^\circ$ are depicted in Figure 9. Additionally, lift coefficients decrease with the Reynolds number. The prolate particles, especially those with $w = 5$, are more significantly affected. Both prolate and oblate particles experience enhanced lift coefficients as w deviates from unity, and $C_{L,\alpha=45^\circ}/C_{L,\alpha=45^\circ,Re_p=10}$ increases with w . The proposed empirical formula accurately predicts lift coefficients with an average error of less than 3%, outperforming previous studies that exhibit larger discrepancies across different flow scenarios.

We further investigate the impact of Mach numbers on the lift force coefficient. Following our analysis of the drag coefficient modifications, we initially conducted Spearman correlation analysis for lift force coefficient. The results, detailed in Table 9, indicate a strong dependence of lift force coefficients on Re_p and M_p , but a much weaker correlation with w .

Similar to drag coefficients, lift coefficients exhibit significant variation at $M_p = 1$. Considering the dependency of lift coefficients on Re_p and M_p , the compressible impact factor is structured as

$$g_l(Re_p, M_p) = l_1 Re_p^{l_2} M_p^{l_3} \quad (23)$$

Henceforth, the lift coefficients of the spheroid particles in compressible flows can be empirically expressed as

$$C_L(Re_p, w, M_p, \alpha) = 2(\sin \alpha)^{c_{i,1}^{Re_p w}} (\cos \alpha)^{c_{i,2}^{Re_p w}} C_{L,\alpha=45^\circ}(Re_p, w) g_l(Re_p, M_p) \quad (24)$$

The parameters in the aforementioned formulas, as given in Table 9, are obtained by data fitting utilizing the numerical simulation results. The average relative error of the proposed formula is less than 4%.

Figures 10 and 11 illustrate the variation of the maximum lift coefficients $C_{L,\alpha=45^\circ}$ with Mach number M_p and Reynolds number Re_p . When Re_p is held constant, the max-

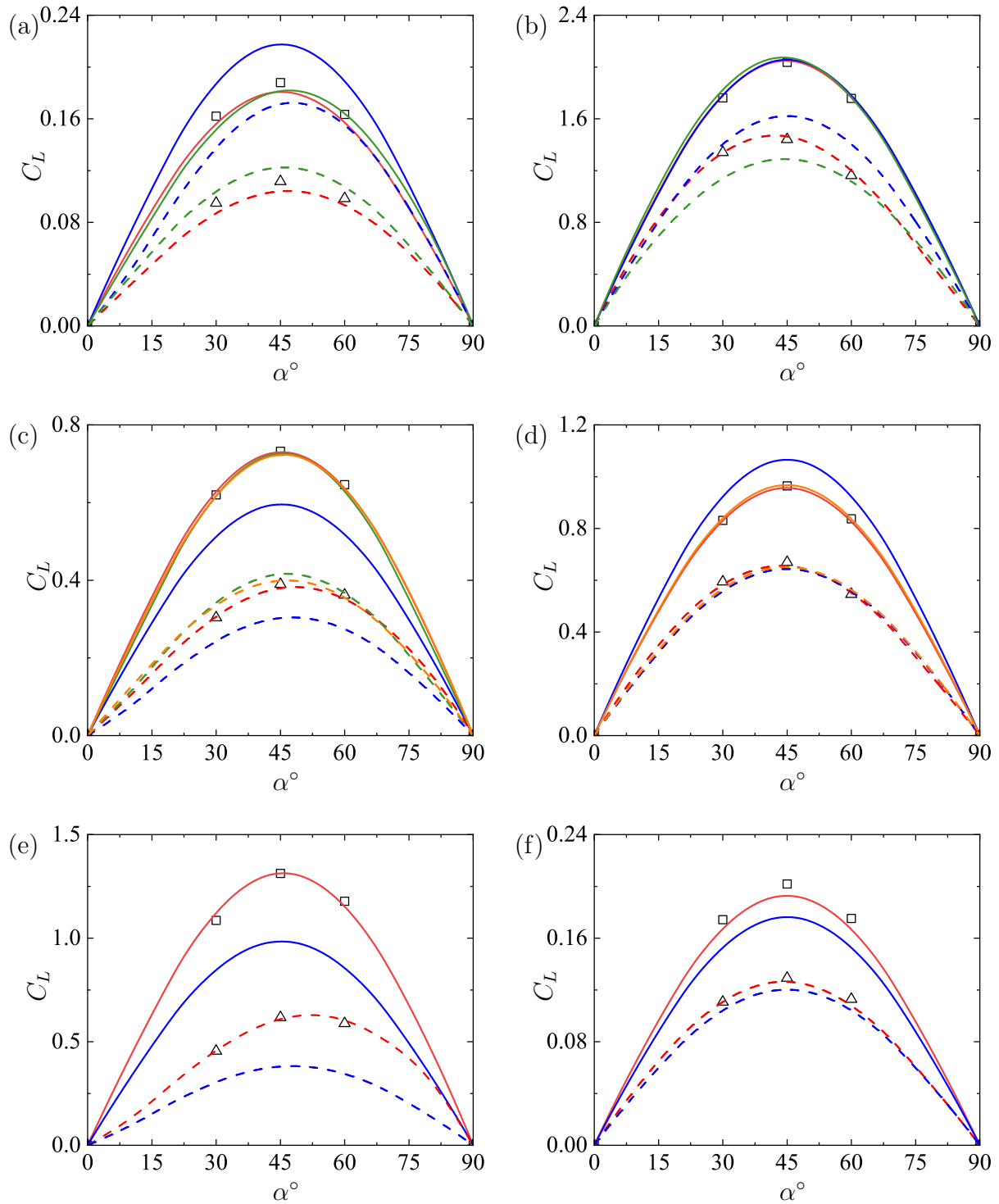


Figure 8: Variation of particle lift force coefficients C_L against α , at $M_p = 0.1$. (a) $w=1.25$, (b) $w=0.2$, (c) $w=2.5$, (d) $w=0.4$, (e) $w=5$, (f) $w=0.8$. Solid lines and square symbols: $Re_p = 10$, dashed lines and triangle symbols: $Re_p = 100$. Symbols: present simulations, red lines: Eq. (22), blue lines: (a,c,e) Ouchene et al. (2016), (b,d,f) Ouchene (2020), green lines: Zastawny et al. (2012), orange lines: Sanjeevi et al. (2018).

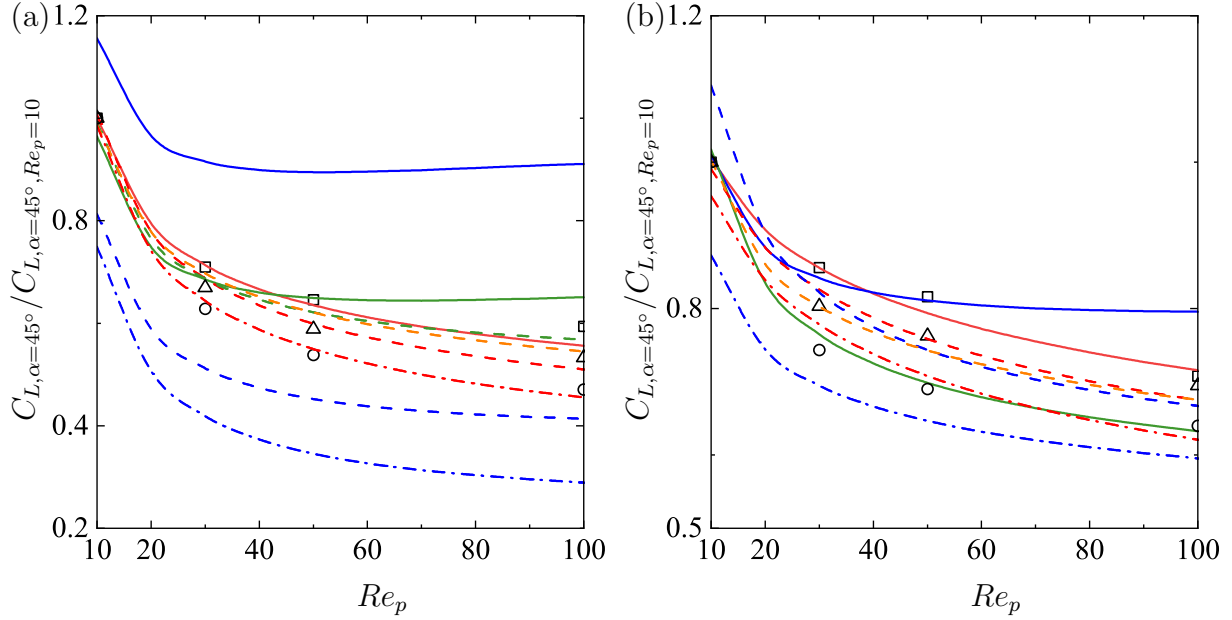


Figure 9: Variation of $C_{L,\alpha=45^\circ}/C_{L,\alpha=45^\circ,Re_p=10}$ against Re_p , at $M_p = 0.1$, (a) $w = 1.25$ (squares and solid lines), $w = 2.5$ (triangles and dashed lines) and $w = 5$ (circles and dash-dotted lines), (b) $w = 0.2$ (squares and solid lines), $w = 0.4$ (triangles and dashed lines) and $w = 0.8$ (circles and dash-dotted lines). Symbols: present simulation, red lines: Eq. (20), blue lines: (a) Ouchene et al. (2016), (b) Ouchene (2020), green lines: Zastawny et al. (2012), orange lines: Sanjeevi et al. (2018).

Table 10: Parameters l_i in Eq.(23) for lift coefficients and average relative error

		l_1	l_2	l_3	Average relative error(%)
$w > 1$	$M_p \leq 1$	1	0.1031	2.546	4.10
	$M_p > 1$	0.5982	0.237	-0.3432	
$w < 1$	$M_p \leq 1$	1	0.0896	3.1416	3.77
	$M_p > 1$	0.6129	0.2148	-0.4256	

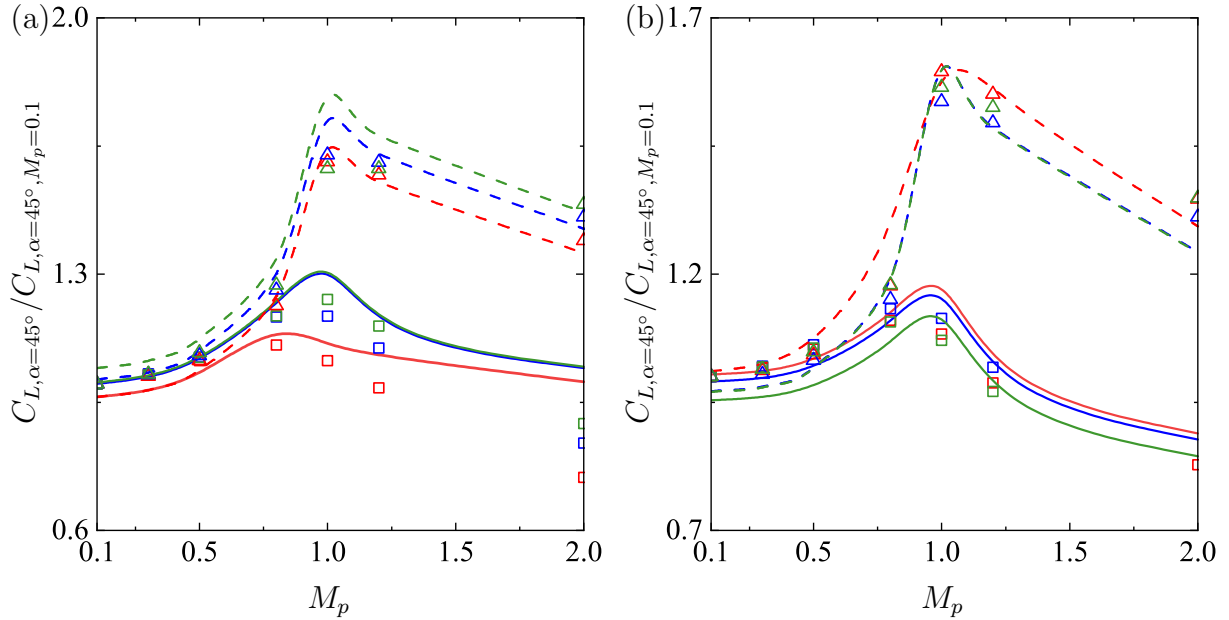


Figure 10: Variation of lift coefficients $C_{L,\alpha=45^\circ}/C_{L,\alpha=45^\circ,M_p=0.1}$ against M_p , (a) prolate particles: $w = 1.25$ (red), $w = 2.5$ (blue), $w = 5$ (green) and (b) oblate particles: $w = 0.2$ (red), $w = 0.4$ (blue), $w = 0.8$ (green). Solid lines and squares: $Re_p = 10$, dashed lines and triangles: $Re_p = 100$. Lines: Eq. (24), symbols: present simulations.

imum lift coefficients initially rise at $M_p < 1$, peak around $M_p \approx 1$, and then decline beyond $M_p = 1$, partially mirroring the behavior of drag coefficients discussed earlier. At a fixed Mach number M_p , the maximum lift coefficients $C_{L,\alpha=45^\circ}$ exhibit a monotonic decrease with Re_p for prolate particles. This trend is prominent in subsonic scenarios but diminishes in supersonic flows. Conversely, for oblate particles, the maximum lift coefficient $C_{L,\alpha=45^\circ}$ decreases solely with Re_p in subsonic conditions at $M_p = 0.3$, while this decreasing trend disappears in transonic and supersonic cases. The proposed formula provides reasonably accurate predictions in terms of Re_p and M_p , except for extreme cases with low Re_p but high M_p , as depicted in Figure 11. In such instances, rarefaction effects cannot be overlooked, rendering both simulations and empirical formulas unsuitable. However, in point-particle simulations within turbulence, such scenarios are infrequent, as Re_p and M_p typically increase concurrently. This observation holds for drag forces as well. The exploration of rarefaction effects falls outside the scope of this paper and will be considered in our future investigation.

In Figure 12, we present the variation of the lift coefficients with the angle of attack α at Mach numbers $M_p = 0.3, 1.0$, and 2.0 , and Reynolds numbers $Re_p = 10$ and 100 . The trend of variation resembles that of incompressible flow. The lift coefficient curves exhibit a slight shift to the right for prolate particles and to the left for oblate particles, a

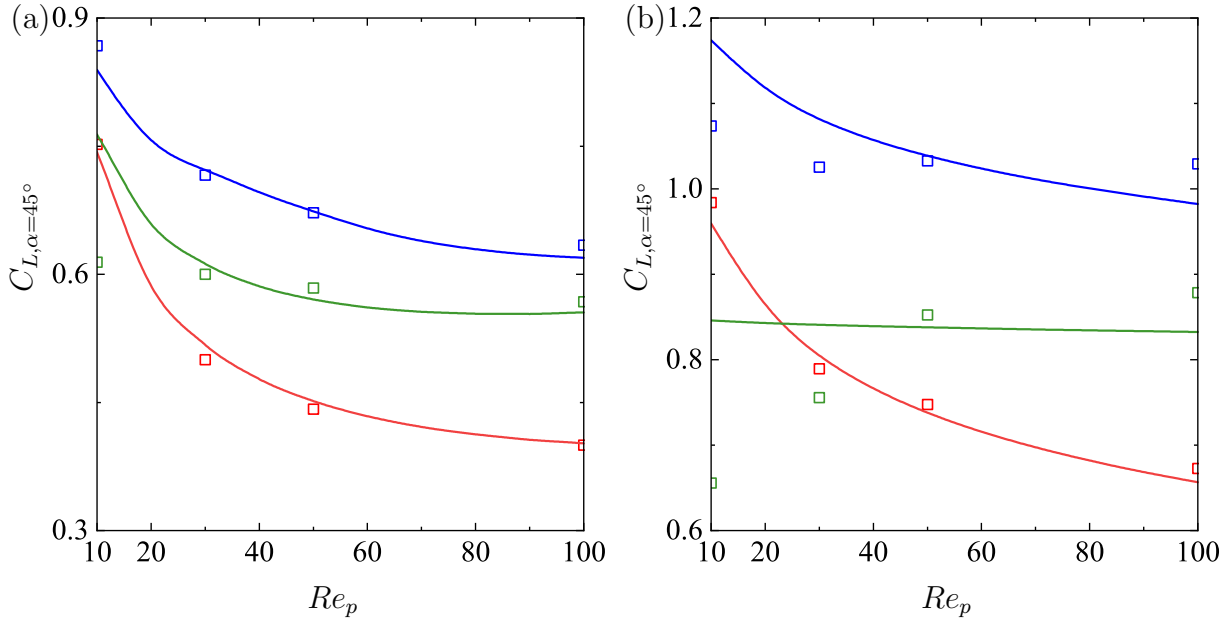


Figure 11: Variation of lift coefficients $C_{L,\alpha=45^\circ}$ against Re_p , (a) $w = 2.5$ and (b) $w = 0.4$. Red: $M_p = 0.3$, blue: $M_p = 1$, green: $M_p = 2$. Lines: Eq. (24), symbols: present simulations.

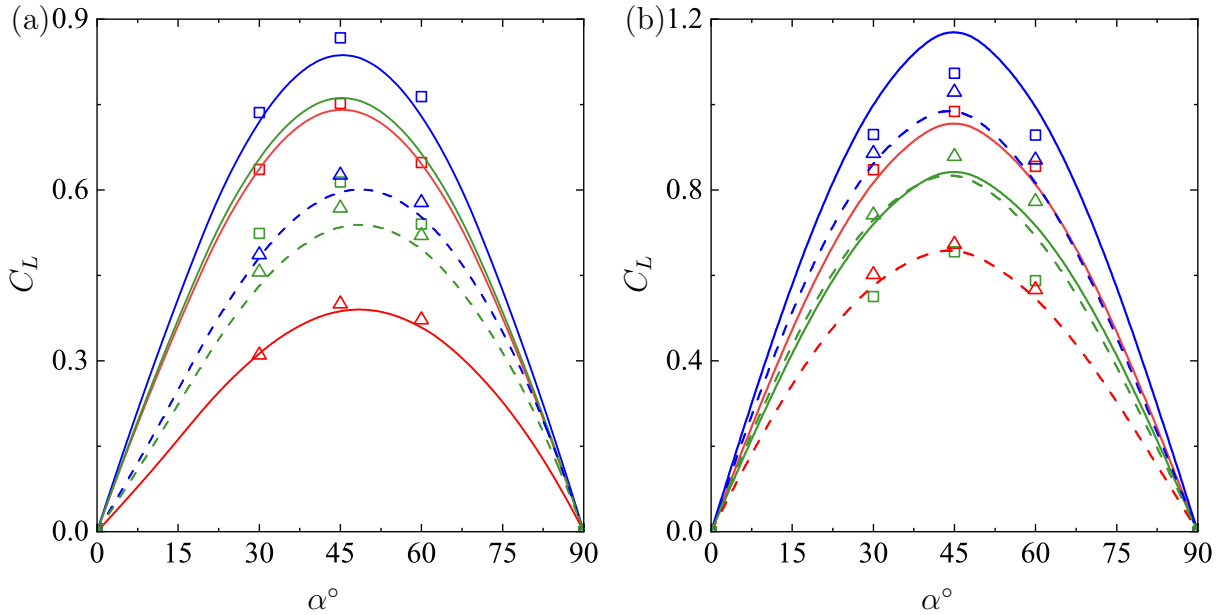


Figure 12: Variation of lift coefficients C_L against α , (a) $w = 2.5$, (b) $w = 0.4$. Solid lines and squares: $Re_p = 10$, dashed lines and triangles: $Re_p = 100$. Red: $M_p = 0.3$, blue: $M_p = 1$, green: $M_p = 2$. Lines: Eq. (24), symbols: present simulations.

pattern well-captured by the proposed empirical formula. Particularly, the relative error for the lift coefficients of oblate particles at $Re_p = 10$ and $M_p = 2.0$ is comparatively high. These discrepancies can be neglected, for as we have stated in the previous subsection, the high M_p and low Re_p correspond to the high particle Knudsen number in such cases, rendering the results meaningless.

This analysis demonstrates that the variation of lift coefficients with angle of attack at different Mach numbers is similar to that of incompressible flow. The lift force coefficients for prolate spheroidal particles exhibits a slight rightward shift, whereas that for oblate spheroidal particles displays a slight leftward shift. When considering Reynolds numbers at 10 and 100 for analysis and comparison, at higher Reynolds numbers, the lift coefficients are notably lower than the lift coefficients at lower Re_p . This discrepancy diminishes gradually with an increase in Mach number.

In this section, we initially refined the lift coefficient for incompressible flows by analyzing cases at low Mach numbers and incorporating asymmetrical distributions with respect to the attack angle. Subsequently, we considered the effects of compressibility for higher Mach number cases and elucidated the formulation of the compressibility factor as a function of both Re_p and M_p . Through a comparison of numerical simulation databases, we have demonstrated that the current proposed formula for the lift coefficient provides accurate results, except in scenarios of high M_p and low Re_p where rarefaction effects become significant.

3.3. Pitching torque

In this subsection, we consider the pitching torque coefficients. Unlike drag and lift forces, pitching torques in creeping flows lack exact solutions, with low Reynolds numbers suggesting zero pitching torque. Empirical formulas are scarce at higher Reynolds numbers. Zastawny et al. (2012) highlighted the similarity between pitching torque coefficients and lift coefficients, leading to the modeling of pitching torque coefficients based on a formula akin to lift coefficients. Ouchene et al. (2016) refined the formula to accommodate higher Reynolds numbers and broader aspect ratios, focusing solely on the prolate spheroid formulation in this study. Subsequently, Ouchene (2020) extended this analysis to oblate spheroidal particles. Building on prior research, the expression for pitching torque coefficients will be determined in conjunction with the lift coefficient expression in the current study, with that of prolate particles as

$$C_{T,\alpha=45^\circ}(Re_p, w) = (C_{D,Stokes,\alpha=90^\circ} - C_{D,Stokes,\alpha=0^\circ})f_{t,\alpha=45^\circ}(Re_p, w) \quad (25)$$

with the factor $f_{t,\alpha=45^\circ}$ cast as

$$f_{t,\alpha=45^\circ}(Re_p, w) = c_{t,3}Re_p^{c_{t,4}+c_{t,5} \ln w} w^{c_{t,6}+c_{t,7}Re_p}. \quad (26)$$

Table 11: Parameters $c_{t,i}$ in Eq. (26) and Eq. (27).

	$i = 1$	$i = 2$	$i = 3$	$i = 4$	$i = 5$	$i = 6$	$i = 7$
$w > 1$	1.0001	0.9999	0.7095	0.7609	-0.0087	0.0	0.0
$w < 1$	0.9995	1.0005	0.1963	0.9024	-0.0056	0.3346	-0.0014

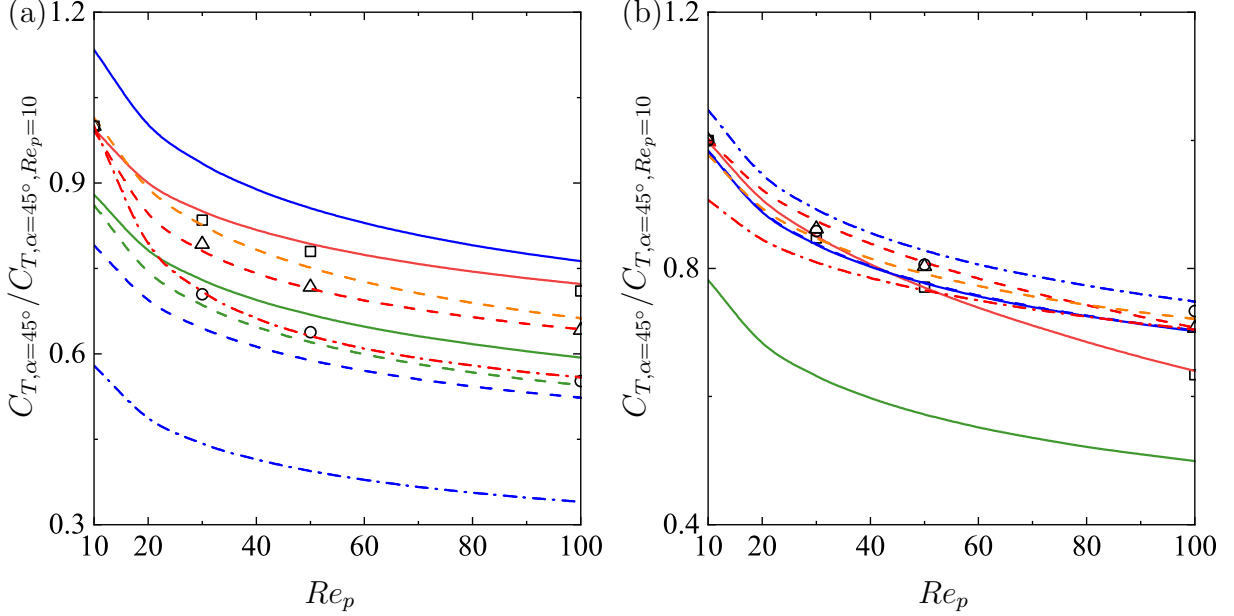


Figure 13: Variation of $C_{T, \alpha=45^\circ} / C_{T, \alpha=45^\circ, Re_p=10}$ against Re_p , at $M_p = 0.1$. (a) $w = 1.25$ (squares and solid lines), $w = 2.5$ (triangles and dashed lines) and $w = 5$ (circles and dash-dotted lines), (b) $w = 0.2$ (squares and solid lines), $w = 0.4$ (triangles and dashed lines) and $w = 0.8$ (circles and dash-dotted lines). Symbols: present simulation, red lines: Eq. (25), blue lines: (a) Ouchene et al. (2016), (b) Ouchene (2020), green lines: Zastawny et al. (2012), orange lines: Sanjeevi et al. (2018).

The pitching torque coefficient can be obtained at varying attack angles by employing the following formula

$$C_T(Re_p, w, \alpha) = 2(\sin \alpha)^{c_{t,1}^{Re_p w}} (\cos \alpha)^{c_{t,2}^{Re_p w}} C_{T, \alpha=45^\circ}(Re_p, w). \quad (27)$$

The w should be replaced with $1/w$ for oblate particles. The variation with the attack angle is expressed using a combination of trigonometric functions. The pitching torque is zero for spherical particles in a uniform flow at relatively low Reynolds numbers, which results in a zero value for C_T as Re_p approaches zero. The parameters included in the equations above are listed in Table 11, calculated using the results of cases at $M_p = 0.1$.

Figure 13 demonstrates that pitching torque coefficients C_T decrease monotonically with Reynolds number at an attack angle of $\alpha = 45^\circ$, similar to the trend observed for lift coefficients. At a given Re_p , C_T is higher as the aspect ratio deviates from 1.0. Comparative analysis with empirical formulas from previous studies (Ouchene et al., 2016;

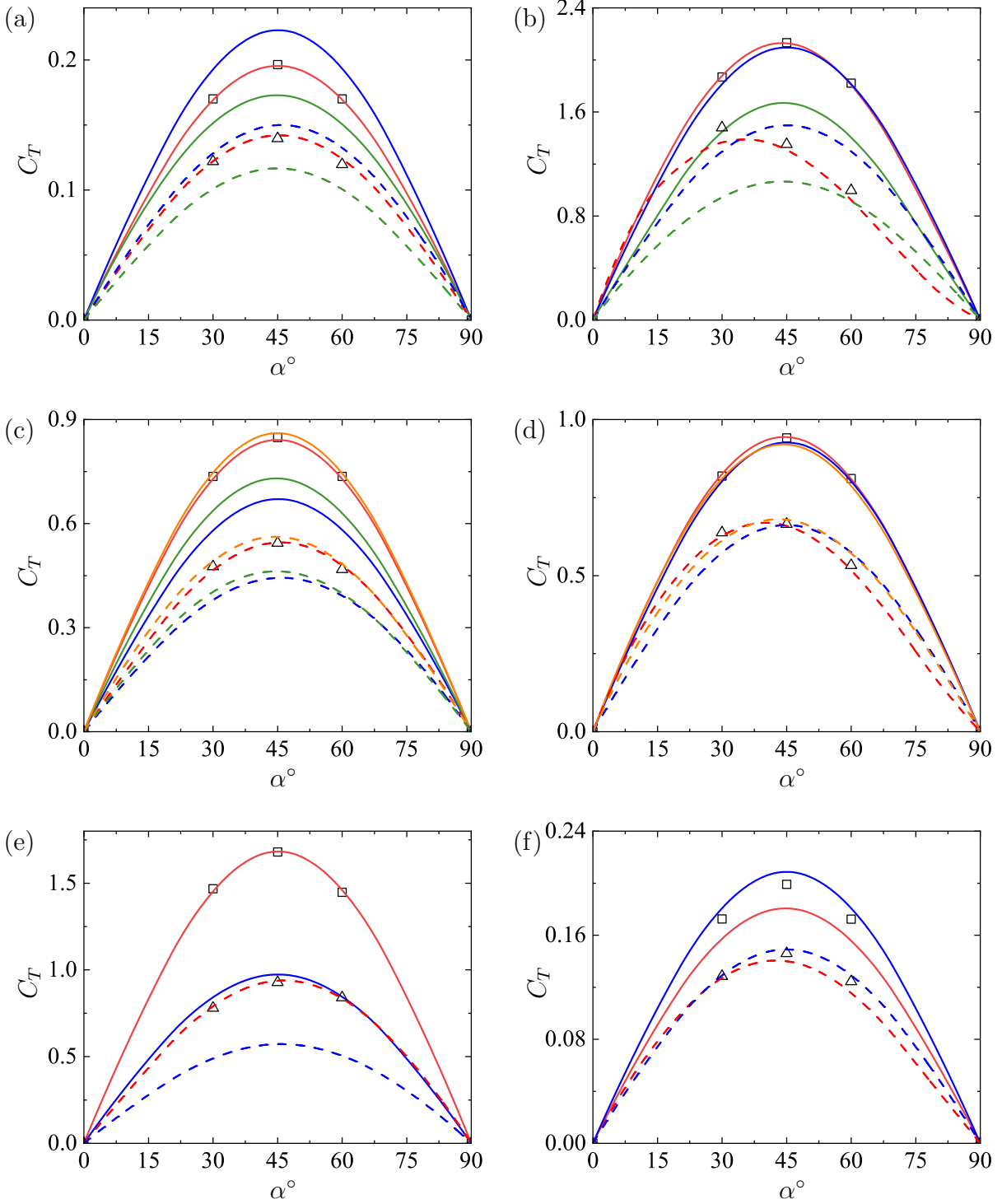


Figure 14: Variation of particle pitching torque C_T coefficients against α , at $M_p = 0.1$. (a) $w = 1.25$, (b) $w = 0.2$, (c) $w = 2.5$, (d) $w = 0.4$, (e) $w = 5.0$, (f) $w = 0.8$. Solid lines and squares: $Re_p = 10$, dashed lines and triangles: $Re_p = 100$. Symbols :present simulation, red lines: Eq. (27), blue lines: (a,c,e) Ouchene et al. (2016), (b,d,f) Ouchene (2020), green lines: Zastawny et al. (2012), orange lines: Sanjeevi et al. (2018).

Table 12: Parameters in Eq.(28) for pitching torque coefficients C_T and average relative error

		t_1	t_2	t_3	t_4	Average relative error(%)
$w > 1$	$M_p \leq 0.8$	1	0.0491	0.1714	2.2645	4.18
	$M_p > 0.8$	0.3409	1	0.2368	-1.2401	
$w < 1$	$M_p \leq 0.8$	1	0.0331	0.1548	2.0034	5.03
	$M_p > 0.8$	0.3398	1	0.2343	-1.1002	

Sanjeevi et al., 2018; Zastawny et al., 2012) reveals that the currently proposed formula exhibits the lowest relative errors. In Figure 14, we further explore the variation of C_T with the attack angle α , comparing predictions from the proposed formula in this study with those of Ouchene (2020); Ouchene et al. (2016); Zastawny et al. (2012) and Sanjeevi et al. (2018). Overall, the variation of C_T follows a similar pattern to that of lift coefficients, with asymmetrical distributions, particularly notable for oblate particles. The proposed formula provides the most precise predictions, with an average relative error of approximately 1.39%.

The compressibility impact factor for the C_T is similar to the drag and lift coefficients in compressible flow, in that the Spearman correlation analysis also show that the C_T is monotonically correlated with Re_p and M_p (not shown here for brevity). However, it is noteworthy that the C_T peaks around $M_p \approx 0.8$, and thus the segmentation was determined to be at $M_p = 0.8$.

$$g_t(Re_p, M_p) = t_1(t_2 Re_p)^{t_3 M_p^{t_4}}. \quad (28)$$

With such refinement, the pitching torque coefficient for spheroidal particles in compressible flows can be written as

$$C_T(Re_p, w, M_p, \alpha) = 2(\sin \alpha)^{c_{t,1}^{Re_p w}} (\cos \alpha)^{c_{t,2}^{Re_p w}} C_{T,\alpha=45^\circ}(Re_p, w) g_t(Re_p, M_p) \quad (29)$$

The parameters in the equation above is reported in Table 12. Compared with the numerical simulation databases, the presently proposed formula predicts C_T with high accuracy, showing a relative error of approximately 4.6%.

The details of the comparison are given as follows. Figures 15 and 16 illustrate the variation of pitching torque coefficients C_T with Mach number M_p and Reynolds number Re_p , respectively. For a constant Reynolds number $Re_p = 10$, the C_T of prolate and oblate particles decreases monotonically until $M_p = 1.2$, beyond which the variation becomes insignificant across all six groups with different aspect ratios. However, at $Re_p = 100$, the C_T increases, peaks at $M_p = 0.8$, and then decreases at higher M_p . Conversely, for a fixed $M_p = 0.3$, the C_T decreases monotonically with Reynolds number Re_p . In transonic

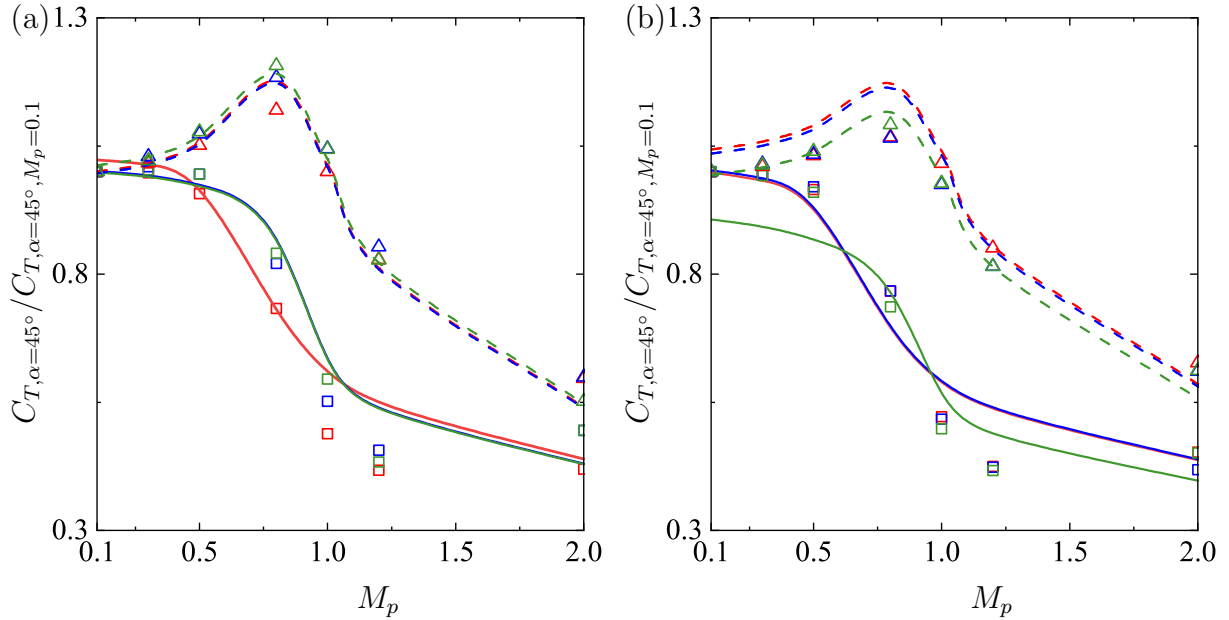


Figure 15: Variation of pitching torque coefficients $C_{T,\alpha=45^\circ}/C_{T,\alpha=45^\circ,M_p=0.1}$ against M_p , (a) prolate particles: $w = 1.25$ (red), $w = 2.5$ (blue), $w = 5$ (green) and (b) oblate particles: $w = 0.2$ (red), $w = 0.4$ (blue), $w = 0.8$ (green). Solid lines and squares: $Re_p = 10$, dashed lines and triangles: $Re_p = 100$. Lines: Eq. (29), symbols: present simulations.

cases at $M_p = 0.8$, the C_T initially increases and then decreases, peaking at $Re_p = 30$. In supersonic cases at $M_p = 2.0$, the C_T are minimally affected by Reynolds number, indicating the significant influence of detached shock waves in these scenarios. Figure 17 showcases the variation of the pitching torque coefficient with angle of attack at different Mach numbers, demonstrating a consistent trend across higher Mach numbers, with a peak at $\alpha = 45^\circ$ and slight asymmetrical distributions. The empirical formula proposed herein effectively captures the trend of variation and provides relatively accurate results for all cases.

4. Conclusion

In this research, we investigate the drag and lift forces and pitching torque of spheroidal particles in compressible uniform flows at various Reynolds and Mach numbers. The aim is to propose empirical formulas for point-particle simulations in high-speed flow applications. Both prolate and oblate particles are examined, encompassing aspect ratios ranging from 0.2 to 5.0, at Reynolds numbers from 10 to 100 and Mach numbers from 0.1 to 2.0, covering subsonic to supersonic flows without shedding vortices. Through an analysis of approximately one thousand numerical simulation cases, we refine empirical formulas for drag and lift forces and pitching torque coefficients, particularly focusing on

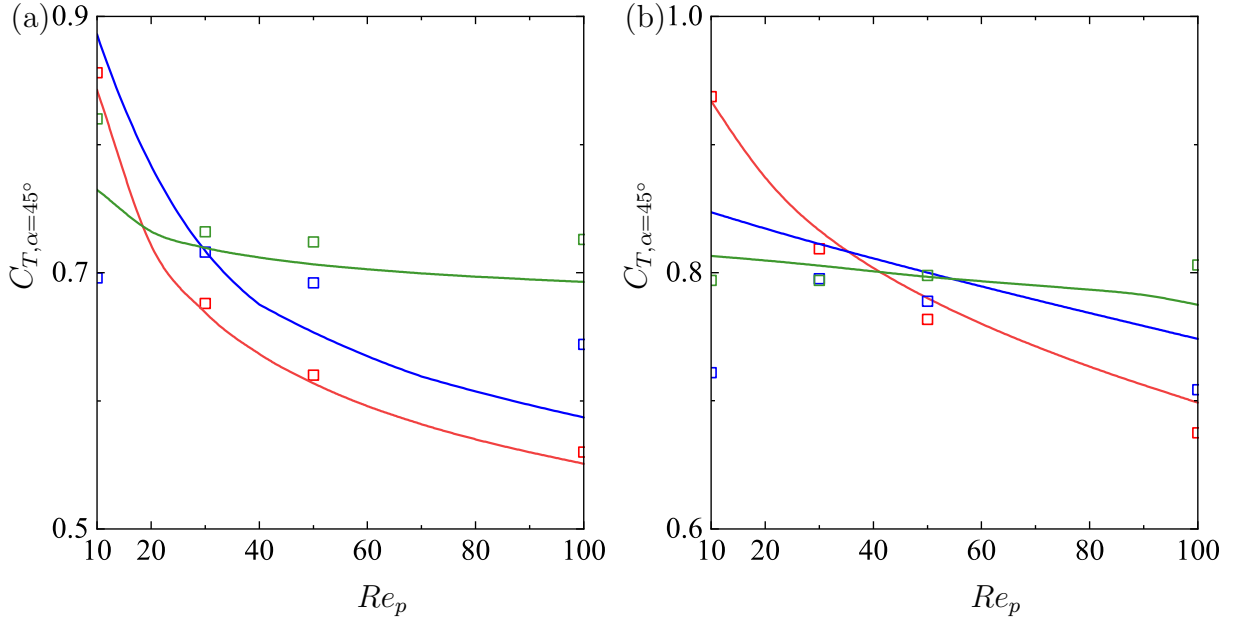


Figure 16: Variation of pitching torque coefficients $C_{T, \alpha=45^\circ}$ against Re_p (When $M_p = 2$, we add 0.4 to $C_{T, \alpha=45^\circ}$), (a) $w = 2.5$ and (b) $w = 0.4$. Red: $M_p = 0.3$, blue: $M_p = 0.8$, green: $M_p = 2$. Lines: Eq. (29), symbols: present simulations.

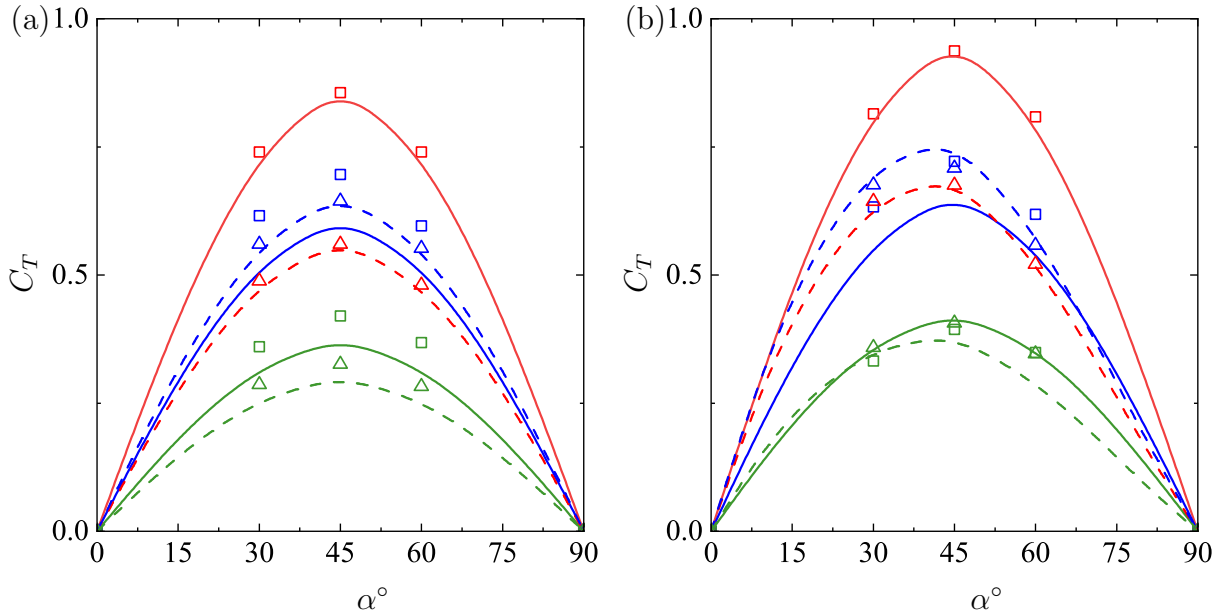


Figure 17: Variation of pitching torque coefficients C_T against α , (a) $w = 2.5$, (b) $w = 0.4$. Solid lines and squares: $Re_p = 10$, dashed lines and triangles: $Re_p = 100$. Red: $M_p = 0.3$, blue: $M_p = 0.8$, green: $M_p = 2$. Lines: Eq. (29), symbols: present simulations.

improvements at low Mach number limits compared to previous studies. Additionally, Spearman correlation analysis highlights the significance of Reynolds and Mach numbers in compressible flow cases, leading to the proposal of compressibility impact factors to enhance incompressible flow formulas. Comprehensive comparisons demonstrate that the proposed empirical formulas yield accurate predictions, with average relative errors below 5% compared to numerical simulation results.

This study addresses the gap in force and torque modeling of spheroidal particles in compressible flow and extends the applicability of the point-particle approach to a broader range of flow conditions. Future research will concentrate on refining the formulas at higher Reynolds numbers to explore unsteady vortex shedding and at low Reynolds numbers but high Mach numbers where rarefaction effects become significant.

References

- Arcen, B., Ouchene, R., Khalij, M., Tanière, A., 2017. Prolate spheroidal particles' behavior in a vertical wall-bounded turbulent flow. *Phys. Fluids* 29, 093301.
- Bailey, A.B., Starr, R.F., 1976. Sphere drag at transonic speeds and high Reynolds numbers. *AIAA J.* 14, 1631–1631.
- Batchelor, G.K., 1970. The stress system in a suspension of force-free particles. *J. Fluid Mech.* 41, 545–570.
- Bounoua, S., Bouchet, G., Verhille, G., 2018. Tumbling of Inertial Fibers in Turbulence. *Phys. Rev. Lett.* 121, 124502.
- Brenner, H., 1961. The Oseen resistance of a particle of arbitrary shape. *J. Fluid Mech.* 11, 604.
- Brenner, H., 1964. The Stokes resistance of an arbitrary particle—III. *Chem. Eng. Sci.* 19, 631–651.
- Capecelatro, J., Wagner, J., 2024. Gas–particle dynamics in high-speed flows. *Annu. Rev. Fluid Mech.* 56, 379–403.
- Clift, R., Gauvin, W.H., 1971. Motion of entrained particles in gas streams. *Can. J. Chem. Eng.* 49, 439–448.
- Cui, Z., Qiu, J., Jiang, X., Zhao, L., 2023. Effect of fluid inertial torque on the rotational and orientational dynamics of tiny spheroidal particles in turbulent channel flow. *J. Fluid Mech.* 977, A20.
- Fröhlich, K., Meinke, M., Schröder, W., 2020. Correlations for inclined prolates based on highly resolved simulations. *J. Fluid Mech.* 901, A5.
- Gustavsson, K., Einarsson, J., Mehlig, B., 2014. Tumbling of Small Axisymmetric Particles in Random and Turbulent Flows. *Phys. Rev. Lett.* 112, 014501.

- Happel, J., Brenner, H., 1983. Low Reynolds number hydrodynamics: with special applications to particulate media. volume 1. Springer Netherlands.
- He, X., Zhao, Z., Ma, R., Wang, N., Zhang, L., 2016. Validation of hyperflow in subsonic and transonic flow. *Acta Aerodyn.Sin.* 34, 267–275.
- Huang, H., Yang, X., Krafczyk, M., Lu, X., 2012. Rotation of spheroidal particles in Couette flows. *J. Fluid Mech.* 692, 369–394.
- Hölzer, A., Sommerfeld, M., 2008. New simple correlation formula for the drag coefficient of non-spherical particles. *Powder Technol.* 184, 361–365.
- Loth, E., 2008. Drag of non-spherical solid particles of regular and irregular shape. *Powder Technol.* 182, 342–353.
- Loth, E., Tyler Daspit, J., Jeong, M., Nagata, T., Nonomura, T., 2021. Supersonic and Hypersonic Drag Coefficients for a Sphere. *AIAA J.* , 3261–3274.
- Marchioli, C., Zhao, L., Andersson, H.I., 2016. On the relative rotational motion between rigid fibers and fluid in turbulent channel flow. *Phys. Fluids* 28, 013301.
- Nagata, T., Nonomura, T., Takahashi, S., Mizuno, Y., Fukuda, K., 2016. Investigation on subsonic to supersonic flow around a sphere at low Reynolds number of between 50 and 300 by direct numerical simulation. *Phys. Fluids* 28, 056101.
- Oberbeck, A., 1876. lieber stationäre Müßigkeitsbewegungen mit Berücksichtigung der inneren Keibung. *J. Reine Angew. Math.* 81, 62–90.
- Ouchene, R., 2020. Numerical simulation and modeling of the hydrodynamic forces and torque acting on individual oblate spheroids. *Phys. Fluids* 32, 073303.
- Ouchene, R., Khalij, M., Arcen, B., Tanière, A., 2016. A new set of correlations of drag, lift and torque coefficients for non-spherical particles and large Reynolds numbers. *Powder Technol.* 303, 33–43.
- Ouchene, R., Khalij, M., Tanière, A., Arcen, B., 2015. Drag, lift and torque coefficients for ellipsoidal particles: From low to moderate particle Reynolds numbers. *Comput. Fluids* 113, 53–64.
- Parmar, M., Haselbacher, A., Balachandar, S., 2010. Improved Drag Correlation for Spheres and Application to Shock-Tube Experiments. *AIAA J.* 48, 1273–1276.
- Richter, A., Nikrityuk, P., 2013. New correlations for heat and fluid flow past ellipsoidal and cubic particles at different angles of attack. *Powder Technol.* 249, 463–474.
- Richter, A., Nikrityuk, P.A., 2012. Drag forces and heat transfer coefficients for spherical, cuboidal and ellipsoidal particles in cross flow at sub-critical Reynolds numbers. *Int. J. Heat Mass Transfer* 55, 1343–1354.
- Rosén, T., Lundell, F., Aidun, C.K., 2014. Effect of fluid inertia on the dynamics and scaling of neutrally buoyant particles in shear flow. *J. Fluid Mech.* 738, 563–590.
- Sanjeevi, S., Kuipers, J., Padding, J.T., 2018. Drag, lift and torque correlations for non-spherical particles from Stokes limit to high Reynolds numbers. *Int. J. Multiphase Flow*

106, 325–337.

- Sanjeevi, S., Padding, J., 2017. On the orientational dependence of drag experienced by spheroids. *J. Fluid Mech.* 820, R1.
- Schiller, L., Naumann, A., 1933. Über die Grundlegenden Berechnungen bei der Schwerkraftaufbereitung *Zeitschrift des Vereines Deutscher Ingenieure.* Ver. Deut. Ing. 77, No. 12.
- Stokes, G., 1901. *Mathematical and physical papers.* volume 3.
- Zastawny, M., Mallouppas, G., Zhao, F., Van Wachem, B., 2012. Derivation of drag and lift force and torque coefficients for non-spherical particles in flows. *Int. J. Multiphase Flow* 39, 227–239.
- Zhao, F., George, W.K., Van Wachem, B.G.M., 2015. Four-way coupled simulations of small particles in turbulent channel flow: The effects of particle shape and Stokes number. *Phys. Fluids* 27, 083301.
- Zhao, L., Marchioli, C., Andersson, H.I., 2014. Slip velocity of rigid fibers in turbulent channel flow. *Phys. Fluids* 26, 063302.